Journal of Hazardous Materials Advances 22 (2026) 101239

Contents lists available at ScienceDirect

Journal of Hazardous Materials Advances

journal homepage: www.elsevier.com/locate/hazadv

Chlorpyrifos degradation by *Zhihengliuella* sp. ISTPL4: An esterase-driven actinobacterial platform for organophosphorus bioremediation

Himanshi Aggarwal [a], Divya Chaudhary [a], Taruna Kumari [b], Nischal Pradhan [c], Vaibhav Mishra [i], Antresh Kumar [d], Anamika Singh [e], Ashutosh Pandey [f], Navaneet Chaturvedi [c], Laurent Dufossé [h,*], Arti Mishra [g,*], Naveen Chandra Joshi [a,*]

[a] *Amity Institute of Microbial Technology, Amity University Uttar Pradesh-201313, India*
[b] *Discipline of Statistics, School of Sciences, Indira Gandhi National Open University, New Delhi, 110068, India*
[c] *Amity Institute of Biotechnology, Amity University Uttar Pradesh-201313, India*
[d] *Department of Biochemistry, Central University of Haryana, Mahendergarh-123031, India*
[e] *Department of Botany, Maitreyi College, University of Delhi, India*
[f] *National Institute of Plant Genome Research, Aruna Asaf Ali Marg, New Delhi 110067, India*
[g] *Department of Botany, Hansraj College, University of Delhi, India*
[h] *Laboratoire CHEMBIOPRO (Chimie et Biotechnologie des Produits Naturels), ESIROI Agroalimentaire, Université de la Réunion, 15 Avenue René Cassin—CS 92003, Saint-Denis Cedex 09, 97744 La Réunion, France*
[i] *Faculty of Science, BioNEST-BHU, Banaras Hindu University, Varanasi, 221005, India*

ARTICLE INFO

Keywords:
Bioremediation
Chlorpyrifos
Esterase
Molecular docking
Organophosphorus pesticide
Enzymatic degradation

ABSTRACT

Organophosphorus pesticides (OPs) are widely used agrochemicals that pose serious risks to the environmental and human health due to their persistence and toxicity. This study reports, for the first time, chlorpyrifos (CPF) degradation by actinobacterium *Zhihengliuella* sp. ISTPL4. Strain ISTPL4 utilized various OPs, including dimethoate, monocrotophos, CPF, and malathion, with the highest growth observed in the presence of CPF as the sole carbon and energy source. Optimal growth and degradation occurred at 28 °C, pH 5, and 3% inoculum in minimal salt medium (MSM). Under optimized conditions, strain ISTPL4 degraded 76.95% of 600 mg L^{-1} CPF within 7 days. GC-MS analysis identified benzene, 1,3-bis(1,1-dimethylethyl) and phenol, 2,4-bis(1,1-dimethylethyl) as intermediates without the formation of toxic metabolite 3,5,6-trichloro-2-pyridinol (TCP). Whole genome analysis revealed five putative esterase genes potentially associated with CPF degradation. Molecular docking identified carboxylesterase B as the most favorable CPF-binding enzyme, while molecular dynamics simulations supported the stability of the enzyme-substrate complex. A putative metabolic pathway for CPF degradation by strain ISTPL4 was proposed. These findings highlight the potential of *Zhihengliuella* sp. ISTPL4 as a promising candidate for sustainable bioremediation of OP-contaminated environments.

1. Introduction

Organophosphorus pesticides (OPs) are highly toxic and pose significant risks to both human health and the environment. OPs are more effective, have a shorter half-life in the environment, and are increasingly utilized in place of carbamates and organochlorines in the agricultural sector. These broad-spectrum pesticides account for approximately 38% of global pesticide usage (Huang et al., 2021). Commonly used OP compounds for controlling agricultural and household pests include chlorpyrifos (CPF), monocrotophos, and quinalphos. Less than 0.1% of the applied pesticide reaches target pests, while the remainder persists in the environment (Nayak and Solanki, 2021). The World Health Organization considers these pesticides a major global health concern, as they are associated with approximately three million cases of poisoning and 300,000 fatalities each year (Sharma et al., 2020; Yadav et al., 2015). The accumulation of pesticides and their breakdown products in surface soil have a significant impact on soil microbial populations and biochemical processes, such as decomposition, nitrification, nitrogen fixation, and ammonification (WHO, 2020).

Among OPs, CPF is a non-systemic, moderately toxic, and persistent chlorinated compound with broad-spectrum pesticidal activity. It appears as a crystalline substance ranging in color from white to pale

* Corresponding authors.
E-mail addresses: laurent.dufosse@univ-reunion.fr (L. Dufossé), artimishrahrc@gmail.com (A. Mishra), ncjoshi@amity.edu (N.C. Joshi).

https://doi.org/10.1016/j.hazadv.2026.101239
Received 24 February 2026; Received in revised form 13 May 2026; Accepted 17 May 2026
Available online 20 May 2026

yellowish-brown. Its breakdown produces 3,5,6-trichloro-2-pyridinol (TCP), a more toxic compound with antimicrobial properties and greater solubility than CPF (Wołejko et al., 2022). As a preventive measure against termites, CPF is often applied to soil around residential and commercial properties. Its half-life in soil ranges from 10 to 120 days depending on the type of soil, pH, initial concentration, water holding capacity, and carbon content present in the soil (Bhende et al., 2022; Islam and Iyer, 2021). CPF is highly soluble in organic solvents, poorly soluble in water (2 mg L^{-1} at 25 °C), and persistent in soil (Nandhini et al., 2021). Due to its slow degradation, CPF can persist in soil for extended periods, posing serious risks to both human health and the environment. Concerns regarding the short- or long-term consumption of CPF-contaminated food have attracted considerable public attention. The environmental fate of CPF is influenced by its physicochemical attributes and surrounding environmental conditions. CPF inhibits acetylcholinesterase activity by phosphorylating the enzyme at neural synapses and plasma membranes in the nervous system of targeted insects. Consequently, acetylcholine accumulates at the synapse, resulting in insect death (Raj and Kumar, 2022; Greer et al., 2019). In non-targeted species, CPF exposure may cause paralysis, neurological disorders, birth deformities, respiratory difficulties, irritation of the skin, rapid muscular contraction, convulsions, immunodeficiency, and death (Nandi et al., 2022). Therefore, effective remediation of CPF is crucial to reduce its long-term environmental persistence and associated health risks.

Microbial decomposition, chemical breakdown, volatilization, and photolysis are some of the mechanisms known to mitigate the environmental impact of CPF by transforming it into less harmful substances. Most CPF applied to soil biodegrades, volatilizes, or photochemically degrades (Kiran et al., 2025). In addition, bioaccumulation of CPF occurs in fish and other aquatic species through runoff and leaching from treated soils. Biodegradation of CPF through co-metabolism or catabolism is considered an efficient and cost-effective strategy for CPF remediation (Kumar et al., 2022). Various physical, chemical, and biological methods have been employed for the remediation of pesticides. Traditional methods, including incineration, landfilling, and chemical decomposition, are complex and may release toxic gases. To overcome these limitations, several physicochemical methods, such as adsorption (Rodríguez et al., 2018), advanced oxidation processes including the Fenton process (Baştürk and Tulun, 2024), and photocatalytic degradation (Veerakumar et al., 2021), have been explored. However, these methods are often expensive, may damage soil properties, and require sophisticated equipment. Consequently, attention has shifted towards cost-effective and environmentally sustainable approaches, including enzymatic degradation and microbial remediation, in which microbes mineralize or biotransform contaminants (Raffa and Chiampo, 2021). To date, numerous bacterial, fungal, and algal species have been isolated and identified for their ability to degrade CPF. The degradation of CPF by bacterial species generally involves enzymatic hydrolysis mediated by organophosphorus hydrolases, resulting in the formation of less harmful compounds. Several bacterial genera, including *Shewanella, Pseudomonas, Bacillus, Xanthomonas,* and *Klebsiella,* have previously been reported to degrade CPF (Govarthanan et al., 2020; Bosu et al., 2024). Actinobacteria are increasingly recognized as versatile degraders of recalcitrant xenobiotics, including pesticides. They are a group of eubacteria well known for their ability to generate diverse secondary metabolites. Their distinct morphological traits, such as a higher surface-area-to-volume ratio, spore production, EPS production, and filamentous growth, contribute to increased stress resistance and biodegradation potential. Also, actinobacteria possess diverse oxidoreductase systems that facilitate bioremediation processes (Behera and Das, 2023). Several actinobacterial species, such as *Streptomyces praecox* strain SP1 and *Arthrobacter* sp. HM01, have recently been reported for CPF degradation (Mali et al., 2022; Elzakey et al., 2023).

Despite extensive studies on CPF biodegradation, most reported bacterial degradation pathways involve the formation and accumulation of the toxic intermediate TCP, which limits complete detoxification. Additionally, the enzymatic basis of CPF degradation, particularly in actinobacteria, remains insufficiently explored at the genomic and molecular levels. Although several studies have reported CPF-degrading microorganisms, only a few have integrated biodegradation efficiency with enzyme-level insights using combined genomic, docking, and dynamic simulation approaches. Furthermore, CPF degradation under environmentally relevant conditions, particularly by extremophilic or psychrotolerant actinobacteria, remains poorly understood. Previously, strain ISTPL4 demonstrated significant bioremediation potential through the degradation of methyl red dye, phenanthrene, and chromium, indicating its metabolic versatility (Takkar et al., 2022; Mishra et al., 2020; Mishra et al., 2020a). However, despite its broad substrate range, its potential for OP degradation has not yet been explored.

In the current study, the CPF-degrading potential of an actinobacterium *Zhihengliuella* sp. ISTPL4, isolated from the extreme environment of Pangong Lake, Ladakh by Mishra et al. (2020), is investigated. This study addresses the above-mentioned gaps by integrating physiological optimization, GC–MS based metabolite profiling, bioinformatic tools, molecular docking, and molecular dynamics (MD) simulations to elucidate the enzymatic basis of CPF degradation. Notably, this work provides evidence for a potential TCP-independent degradation pathway and identifies esterase enzymes, particularly carboxylesterase B, as key contributors to CPF hydrolysis. Overall, this study provides insight into esterase-mediated CPF degradation in actinobacteria and highlights the potential of strain ISTPL4 for sustainable bioremediation under environmentally relevant conditions.

2. Material and methods

2.1. Chemicals

Four pesticides, namely, malathion, CPF, monocrotophos, and dimethoate, used in the current study were purchased from Sigma-Aldrich, USA. All organic solvents used were of analytical grade.

2.2. Screening for organophosphorus pesticide degradation

Various OPs were screened to determine the degradation capability of *Zhihengliuella* sp. ISTPL4. An overnight-grown culture of strain ISTPL4 in Luria Bertani (LB) medium was used as the inoculum. To investigate the growth of strain ISTPL4 using OPs as the sole carbon source, a 5% (v/v) inoculum was prepared from the overnight-grown culture. The inoculum density was standardized using a 0.5 McFarland turbidity standard, corresponding approximately to $1–2 \times 10^8$ CFU mL^{-1}, and was further verified spectrophotometrically ($OD_{600} \approx 1.0$) to ensure consistency across experiments. The culture was inoculated into 20 mL of minimal salt medium (MSM) containing Na_2HPO_4 (7.8 g L^{-1}), KH_2PO_4 (6.8 g L^{-1}), $MgSO_4$ (0.2 g L^{-1}), $C_6H_8O_7Fe^{3+}{\cdot}yNH_3$ (0.01 g L^{-1}), $Ca(NO_3)_2{\cdot}4H_2O$ (0.05 g L^{-1}), $NaNO_3$ (0.085 g L^{-1}), $CuSO_4{\cdot}5H_2O$ (0.05 g L^{-1}), $MnSO_4{\cdot}H_2O$ (0.04 g L^{-1}), and yeast extract (0.5 g L^{-1}), supplemented with 50 mg L^{-1} of the pesticides, malathion, CPF, monocrotophos, and dimethoate in 100 mL Erlenmeyer flasks. The flasks were incubated at 28 °C on a rotary shaker at 150 rpm. Bacterial growth was monitored every 24 h for 5 days by measuring optical density at 600 nm (OD_{600}) using a UV-1800 Shimadzu spectrophotometer. MSM containing the respective pesticide concentrations without bacterial inoculation served as the control. All experiments were performed in triplicate. The most suitable pesticide for further study was selected based on bacterial growth in the presence of different OPs.

2.3. Optimization of CPF utilization by strain ISTPL4

The growth of strain ISTPL4 was checked under various parameters, including different pH values, temperatures, inoculum concentrations, glucose concentrations, and salt concentrations. An overnight-grown

bacterial culture, standardized spectrophotometrically to $OD_{600} \approx 1.0$, was used as the inoculum, and 5% (v/v) was added to MSM containing varying concentrations of CPF (100 to 1000 mg L^{-1}). The utilization of CPF under different environmental conditions was assessed based on bacterial growth.

Growth was monitored at different temperatures (5 °C, 20 °C, 28 °C, and 37 °C) in MSM. For pH optimization, the pH of the medium was adjusted to 3, 5, 7, 9, and 11 using 1 N NaOH or 1 N HCl. Salt and glucose tolerance was evaluated by supplementing MSM with 1–7% NaCl (w/v) and 1–7% glucose (w/v), respectively, at increments of 2%. Different inoculum concentrations (3%, 5%, 7%, and 10% v/v) were prepared using overnight-grown bacterial cultures, while maintaining a consistent cell density through spectrophotometric adjustment ($OD_{600} \approx 1.0$). Bacterial growth was monitored for 4 days at 24-h intervals by measuring OD_{600}. The optimization outcomes were validated statistically. Predictive models were applied to describe the behavior of bacterial growth under different CPF conditions and optimization conditions, including pH, salt, temperature, glucose concentration, and inoculum size. To analyze the growth rate, two primary sigmoidal growth models, namely the Logistic and Gompertz, were employed (Zwietering et al., 1990). Both models were expressed in terms of microbiologically relevant parameters, including maximum specific growth rate (μ), lag phase duration (λ), and asymptote (A), representing the maximum biomass or carrying capacity. The reparametrized sigmoidal growth models are presented in Eq. (1) and Eq. (2).

$$\text{Logisticmodel} : y = A \Big/ \left\{ 1 + \exp\left[\frac{4\mu}{A}(\lambda - t) + 2 \right] \right\}, \quad (1)$$

and

$$\text{Gompertzmodel} : y = A.\exp\left\{ -\exp\left[\frac{\mu.e}{A}(\lambda - t) + 1 \right] \right\}. \quad (2)$$

The growth models were analyzed using R software (https://www.r-project.org/). Parameter estimates for μ, A, and λ were computed using the 'nls' function with the 'port' algorithm. To visualize the growth phase, the mean OD_{600} values (y) were plotted against time in days (t). A higher value of μ indicated a higher growth rate, while λ reflected the duration of the adaption phase. The goodness of fit of the models was evaluated using the coefficient of determination (R^2).

2.4. GC-MS analysis

Growth of strain ISTPL4 was checked in the presence of 600 mg L^{-1} CPF in a 500 mL Erlenmeyer flask containing 200 mL sterile MSM at 28 °C, pH 5, with 3% inoculum and shaking at 150 rpm for 7 days. MSM containing the same concentration of CPF without bacterial inoculation served as the control. The flasks were incubated at 28 °C and 150 rpm for 7 days. A 20 mL sample was aseptically collected at regular intervals (0, 3, 5, and 7 days) to estimate the concentration of CPF and its metabolites. Bacterial growth was determined by measuring OD_{600}. The samples were centrifuged at 3500 rpm for 20 min (Ambreen and Yasmin, 2021). Ethyl acetate was added to the supernatant at a ratio of 1:2 and shaken for 1 h. The samples partitioned into two layers, and the upper organic layer was collected, evaporated using a rotary evaporator, and dried under a stream of nitrogen gas (Wang et al., 2016). The dried samples were resuspended in 1.5 mL methanol and filtered through 0.45 μm sterile syringe filters to remove particulate matter. The filtered samples were transferred to GC vials for GC–MS analysis.

Untargeted gas chromatography–mass spectrometry (GC–MS) analysis was performed using a Shimadzu Gas Chromatograph (GC-2010 plus) coupled with a mass spectrometer (TQ 8050), autosampler (AOC-20 s), and autoinjector (AOC-20i). Separation was carried out using an SH-Rxi-5Sil MS capillary column (30 m x 0.25 μm, 0.25 mm) (Restek Corporation, USA), with helium as the carrier gas at a flow rate of 1 mL min^{-1}. The GC temperature program consisted of initial heating at 80 °C for 2 min, followed by a temperature ramp rate of 5 °C min^{-1} to 250 °C with a hold time of 2 min, and a final ramp of 10 °C min^{-1}, with a hold time of 24 min. Total run time for GC–MS was 67 min with a solvent delay of 4.5 min. Chromatogram integration and mass spectral analyses were done using Shimadzu LabSolutions software (GC–MS Solution Version 4.53SP1). Metabolites were identified using the NIST17s spectral library (Kundu et al., 2018). All samples, including controls, were processed under identical extraction and analytical conditions to eliminate procedural bias.

The percentage degradation of CPF was calculated using the following equation, where C_i and C_f represent the initial and final concentrations of CPF, respectively.

$$\left(C_i - C_f\right)/C_i \times 100 \quad (3)$$

2.5. Dechlorination assay

The presence of chloride (Cl^-) ions was determined using the argentometric titration method (Mohr's method). A set-up similar to GC-MS analysis was used for this study. Strain ISTPL4 was grown in MSM containing 600 mg L^{-1} CPF for 7 days at pH 7. Cl^- ions were measured on days 0, 3, 5, and 7 following the protocol described by Anomi and Emmanuel (2025).

2.6. Physicochemical properties

Whole-genome sequencing of strain ISTPL4 has previously been reported (Mishra et al., 2018). Genome sequence analysis revealed five putative proteins, namely carboxylesterase B, carboxylesterase NlhH, esterase YbfF, acetylxylan esterase, and phosphotriesterase, potentially involved in CPF degradation. Protein sequences of carboxylesterase B, carboxylesterase NlhH, esterase YbfF, acetylxylan esterase, and phosphotriesterase were retrieved from NCBI. The physicochemical properties of the proteins were analyzed using ExPASy ProtParam server (https://web.expasy.org/protparam), accessible through the Swiss Bioinformatics Resource Portal. The analyzed parameters included molecular weight, theoretical isoelectric point (pI), extinction coefficient, total number of positively and negatively charged residues, instability index, grand average hydropathy (GRAVY), and aliphatic index. Additionally, sequence alignment was performed using Clustal Omega with a representative bacterial α/β hydrolase (WP_003975294.1) to identify conserved catalytic residues characteristic of esterase enzymes.

2.7. Secondary structure prediction

The secondary structures of all five targeted proteins were predicted using SOPMA (Self-Optimized Prediction Method of Alignment) [NPS@: SOPMA secondary structure prediction (ibcp.fr)]. The analysis predicted the percentages of α-helices, β turns, extended strands, and random coils present in the selected proteins. Protein sequences were uploaded to the SOPMA server in the FASTA format for secondary structure analysis.

2.8. Phylogenetic tree

Protein sequences of five esterase enzymes from 10 bacterial species were aligned utilizing Clustal alignment explorer. A neighbor-joining (NJ) phylogenetic tree was constructed using MEGA X software, following the method described by Saitou and Nei (1987). Evolutionary distances were calculated employing the Poisson correction method as described by Tamura et al. (2004). Bootstrap analysis was performed to assess the reliability of the phylogenetic tree.

2.9. Ligand preparation

The three-dimensional structure of CPF was retrieved from PubChem in the SDF format and converted to PDB format using Open Babel, as

PDB format is required for ligand preparation in AutoDock (Trott and Olson, 2010). Hydrogen atoms were added to the ligand using the AutoDock tool, and the prepared ligand structure was exported in PDBQT format for molecular docking analysis.

2.10. Binding site analysis

The CASTp online tool (http://cast.engr.uic.edu) was used to identify and analyze pockets present in the 3D structures of the proteins (Tian et al., 2018). PDB files of the proteins were submitted to the CASTp server to determine the number, surface area, and volume of the predicted active sites.

2.11. Protein modeling of target enzymes

3D structures of five esterase enzymes from strain ISTPL4 were predicted using ColabFold (Mirdita et al., 2022), an accelerated implementation of AlphaFold2 integrated with MMseqs2 for homology searches. The predicted structural models were refined and visualized using ChimeraX, and their stereochemical quality was evaluated using MolProbity.

2.12. Protein preparation and molecular docking

The PDB files of the five receptor proteins were prepared by the AutoDock tool. Receptor preparation involved the removal of non-essential water molecules and heteroatoms, followed by the addition of hydrogen atoms and Kollman charges. The prepared receptor structures were saved in PDBQT format. Grid boxes for docking were defined on the predicted active site regions identified through CASTp analysis. Molecular docking was performed between CPF and five target proteins using AutoDock Vina. Both protein and ligand structures were uploaded in PDBQT format, and docking protocol was executed for each of the targeted protein and ligand. To study the degrading capability, CPF was docked with carboxylesterase B, carboxylesterase NlhH, esterase YbfF, phosphotriesterase, and acetylxylan esterase. Docking log files were analyzed after completion, yielding nine conformations with corresponding binding affinities and RMSD values for each complex. The conformation showing the most negative binding affinity was chosen for further analysis.

2.13. Molecular dynamics (MD) simulation

To explore the structural and dynamic effects of CPF binding on five enzyme receptors—esterase YbfF, carboxylesterase B, carboxylesterase NlhH, acetylxylan esterase, and phosphotriesterase—MD simulations were performed on both ligand-bound (holo) and unbound (apo) forms. These simulations were conducted to assess complex stability, dynamic behavior, and ligand-induced conformational changes. GROMACS version 2021.4 was applied to conduct all simulations (Abraham et al., 2015; Lindahl et al., 2021), employing the CHARMM36m all-atom force field (July 2022 release) for proteins. Ligand topologies were generated using the CGenFF (version 2.5) force field through the ParamChem server (Vanommeslaeghe et al., 2010, 2012).

Each system was solvated using the SPC216 water model inside a cubic periodic box and subsequently neutralized with Na^+ or Cl^- counterions (Berendsen et al., 1981). Before production simulations, all systems underwent energy minimization for 50,000 steps utilizing the steepest descent approach to remove steric conflicts and ensure convergence. The process commenced with a two-step equilibration: an initial NVT phase, maintaining constant Number, Volume, and Temperature for 1000 ps with position restrictions, followed by an NPT phase, ensuring constant Number, Pressure, and Temperature for an additional 1000 ps. Temperature was maintained at 300 K using the V-rescale thermostat, while pressure was regulated at 1 atm using the Parrinello-Rahman barostat. The LINCS algorithm, as described by Hess et al. (1997), was applied to constrain covalent bonds involving hydrogen atoms, allowing the use of a 2 fs integration time step. The Particle Mesh Ewald (PME) method was employed to address electrostatic interactions, utilizing a cutoff of 1.2 nm.

For every system, producing MD simulations were executed for 100 ns for each system and repeated in triplicate to ensure reproducibility. The Verlet cutoff scheme was employed to refresh neighbor lists every 1.0 ps. Initial velocities were assigned according to the Maxwell-Boltzmann distribution at 300 K. The final topology for each system included the protein, the CPF ligand, water molecules, and ions. Ligand topologies were prepared using the CGenFF-compatible ParamChem webserver (https://cgenff.umaryland.edu), where bonded parameters, charges, and dihedral terms were generated and validated before system integration.

Trajectory analyses were conducted utilizing integrated tools of GROMACS, including rms, rmsf, hbond, mindist, cluster, covar, and anaeig. Root Mean Square Deviation (RMSD) and Root Mean Square Fluctuation (RMSF) metrics were used to evaluate global and local flexibility of proteins. Hydrogen bond (H-bond) analysis was performed to quantify ligand-receptor interactions. Principal Component Analysis (PCA) and cluster analysis (0.15 nm cutoff) were used to capture dominant motions and conformational populations. Additionally, projections along the first two principal components were implemented to generate free energy landscapes. Custom Python and shell scripts were used to extract trajectory frames and calculate the percentage occupancy of key hydrogen bonds.

Trajectory visualizations were constructed using VMD 1.9.4 and PyMOL 2.5, while plots were prepared using xmgrace and Matplotlib (Schrödinger, 2020; Humphrey et al., 1996). This simulation strategy provided detailed insight into the binding interactions and dynamic behavior of CPF with different enzymatic targets.

2.14. Free energy calculation

The binding free energy of enzyme-ligand complexes were analyzed using the Molecular Mechanics-Poisson–Boltzmann Surface Area (MM-PBSA) method implemented through the g_mmpbsa tool integrated with GROMACS (Kumari et al., 2014). This method estimates free binding energy by combining molecular mechanics energies with solvation energy terms while excluding entropic terms.

The total binding free energy (ΔG_{bind}) was calculated using the following equation:

$$\Delta G_{bind} = G_{complex} - \left(G_{receptor} + G_{ligand}\right)$$

where $G_{complex}$, $G_{receptor}$, and G_{ligand} represent the free energies of the enzyme-ligand complex, apo enzyme, and unbound ligand, respectively.

Each free energy term was determined using the following equation:

$$G = G_{MM} + G_{Solvation}$$

where G_{MM} represents the molecular mechanics energy, comprising electrostatic interactions ($G_{Coulomb}$) and van der Waals forces (G_{VDW}):

$$G_{MM} = G_{Electrostatic} + G_{VDW}$$

$G_{Solvation}$ represents solvation effects, comprising polar (G_{Polar}) and non-polar ($G_{Nonpolar}$) contributions:

$$G_{Solvation} = G_{Polar} + G_{Nonpolar}$$

The Poisson–Boltzmann (PB) model was used to calculate the polar solvation energy, while the solvent-accessible surface area (SASA) method was used to estimate the non-polar solvation energy.

2.15. Amplification of the carboxylesterase B (Caeb) gene

Genomic DNA of strain ISTPL4 was extracted utilizing a bacterial DNA extraction kit (Qiagen). The concentration and purity of extracted

DNA were assessed using a Nanodrop and visualized on a 0.8% agarose gel using a Gel Doc system (Bio-Rad). To amplify the carboxylesterase B (*Caeb*) gene, the following primers were designed based on the complete gene sequence:

Forward: 5′-GCGAATTCGTGAAGACTCGATCCCTGTCCC-3′
Reverse: 5′-CCCAAGCTTTCACTCGCAGCGCAAGGCCGTC-3′

Primer specificity was validated using NCBI Primer Blast. Gene-specific PCR amplification was performed using a reaction mixture comprising 4 μL HF buffer, 1.2 μL dNTPs, 1 μL forward primer, 1 μL reverse primer, 0.6 μL DMSO, 0.2 μL Phusion polymerase, 11 μL Milli-Q water, and 1 μL DNA template. PCR amplification was carried out in a thermocycler under the following conditions: initial denaturation at 95 °C for 3 min, denaturation at 95 °C for 45 s, annealing at 56 °C for 45 s, extension at 72 °C for 2 min, and final extension at 72 °C for 10 min with 35 cycles run. The amplified PCR product was visualized on 0.8% agarose gel and subsequently purified using a Qiagen gel extraction kit.

3. Results

3.1. Screening of OP utilization

Zhihengliuella sp. ISTPL4 was screened for its ability to utilize four OPs, namely CPF, malathion, monocrotophos, and dimethoate, as sole carbon sources. Among the tested pesticides, the strain showed the highest growth in MSM supplemented with 50 mg L^{-1} CPF (Fig. 1). Growth in the presence of other OPs was comparatively lower. Based on these observations, CPF was selected for further biodegradation studies.

3.2. Optimization of CPF utilization

The growth of strain ISTPL4 was evaluated across different CPF concentrations ranging from 100 to 1000 mg L^{-1}. A sigmoidal growth pattern was observed under all conditions. The growth data were fitted to Logistic and Gompertz models, and model performance was evaluated using R^2 values (Table 1). The Gompertz model exhibited higher R^2 values under several conditions, including at 600 mg L^{-1}, whereas the Logistic model provided a better fit under certain conditions, such as inoculum size and some CPF concentrations. Accordingly, the model with the higher overall R^2 value was considered the better fit for each condition. Although all parameters (μ, λ, and A) were estimated, μ was used as the primary indicator of growth performance under different conditions.

Based on the Gompertz model, the highest growth rate was observed at a CPF concentration of 600 mg L^{-1} (μ = 0.2890873) (Table 1**; Supplementary Fig. S1**), and this concentration was selected for further optimization studies. Under these conditions, the maximum growth rate was recorded at 28 °C (μ = 0.4644297) and pH 5 (μ = 3.0714081) (Table 1; **Supplementary Figs. S2 and S3**). The strain demonstrated growth over a broad pH range (3–11), although reduced growth rate was observed at pH 11. Optimal growth was achieved with a 3% inoculum size (μ = 0.7214560) based on the Logistic model (Table 1; **Supplementary Fig. S4**). In addition, the presence of 1% glucose enhanced growth (μ = 0.5570759), and the strain tolerated salt concentrations up to 7%, with optimal growth observed at 1% salt concentration (μ = 1.6993757) both based on Gompertz model (Table 1; **Supplementary Figs. S5 and S6**). These results demonstrate that strain ISTPL4 exhibits strong adaptability to varying environmental conditions, with optimal growth and CPF utilization occurring under moderately acidic pH, mesophilic temperature, and low salinity conditions.

3.3. Chlorpyrifos metabolite identification

GC–MS analysis was performed to evaluate the metabolites formed and the extent of CPF degradation by strain ISTPL4. Strain ISTPL4 showed 76.95% degradation of 600 mg L^{-1} CPF under optimized conditions within 7 days (Fig. 2**A**). The decrease in CPF concentration over time, as determined by GC–MS analysis, corresponded with a simultaneous increase in bacterial growth (OD_{600}) observed under the same conditions (Fig. 1 **and Supplementary Fig. S1**), providing direct evidence of CPF metabolism rather than mere tolerance. Table 2 summarizes previously reported CPF degradation by different bacterial genera. Among these, *Zhihengliuella* sp. ISTPL4 demonstrated a high potential to utilize CPF. Metabolites formed during CPF utilization were analyzed by GC-MS and are listed in Table 3. A dominant CPF peak with a retention time (RT) of 27.3 min was detected in samples collected on all sampling days **(Supplementary Fig. S7).** The intensity of this peak was highest on day 0 and subsequently decreased on days 3, 5, and 7, indicating progressive utilization of CPF by strain ISTPL4. Library matching identified intermediate metabolites as benzene, 1,3-bis(1,1-dimethylethyl), and phenol, 2,4-bis(1,1-dimethylethyl), with RT values of 10.7 and 17.2 min, respectively (Fig. 2**B**).

No significant reduction in CPF concentration was observed in media containing CPF without bacterial inoculation (abiotic controls), indicating that the degradation was biologically mediated. Importantly, GC–MS analysis of abiotic controls did not show peaks corresponding to the identified metabolites at their respective RT values, indicating that these compounds were not artifacts resulting from the analytical procedure or column bleed **(Supplementary Fig. S8).** Peak intensities of

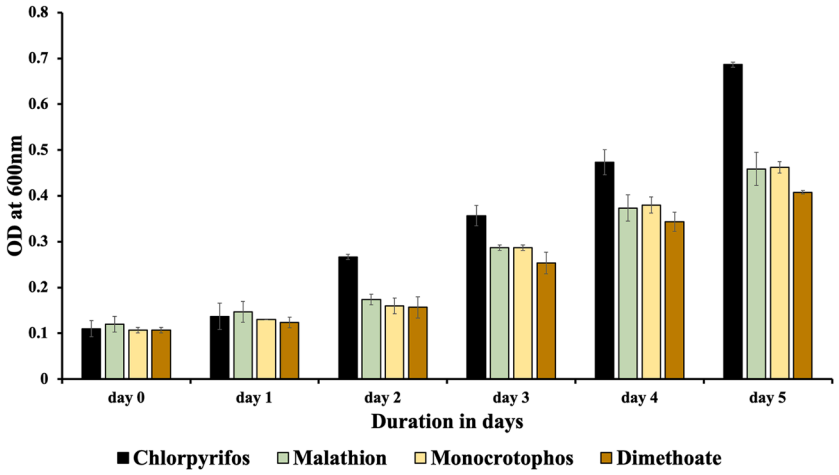

Fig. 1. Organophosphate pesticide utilization. The utilization of different pesticides (chlorpyrifos, malathion, monocrotophos, and dimethoate) by strain ISTPL4 was checked at 50 mg L^{-1} concentration. Data values are shown as mean ± standard deviation (shown by error bars).

Table 1
Fitting of growth data of logistic and Gompertz models.

Conditions	Values	Logistic				Gompertz				Best
		A	μ	λ	R^2	A	μ	λ	R^2	
pH	3	2.4702146	2.4603493	−0.3019718	0.9992989	2.4711353	3.0403932	−0.2522228	0.9993435	Gompertz
	5	**2.5383251**	**2.4924561**	**−0.3017447**	**0.9997375**	**2.5392135**	**3.0714081**	**−0.2533578**	**0.9997674**	**Gompertz**
	7	2.4819948	2.0995149	−0.3553226	0.9987195	2.4838027	2.5316419	−0.3041737	0.9987245	Gompertz
	9	2.3993201	2.2361305	−0.3367065	0.9991747	2.4005918	2.7486490	−0.2809356	0.999247	Gompertz
	11	1.9993130	1.7209940	−0.3879381	0.9975997	1.9995625	2.1349310	−0.3181634	0.9974272	Logistic
Salt (%)	**1**	**2.2998302**	**1.4642460**	**−0.5171361**	**0.9985166**	**2.3077732**	**1.6993757**	**−0.4538016**	**0.9991238**	**Gompertz**
	3	1.9832373	0.6081393	−1.1123343	0.9952845	2.0334649	0.6599938	−1.0365178	0.9913586	Logistic
	5	1.9758537	0.6867134	−1.0802224	0.9941415	2.0056689	0.7709702	−0.9664477	0.9916118	Logistic
	7	2.1392111	0.7500186	−0.9680103	0.9984651	2.1761596	0.8273840	−0.8863862	0.9954959	Logistic
Glucose (%)	**1**	**1.9493376**	**0.4994043**	**−1.5024511**	**0.9908432**	**2.0048188**	**0.5570759**	**−1.3331893**	**0.9949605**	**Gompertz**
	3	1.8560470	0.2908657	−2.3888715	0.9799164	2.0127246	0.3054527	−2.2666274	0.9825258	Gompertz
	5	1.8767981	0.3676093	−2.0803344	0.9868631	1.9555640	0.4065135	−1.8620600	0.9907922	Gompertz
	7	2.0572998	0.3311734	−2.0558346	0.9939955	2.2989595	0.3351206	−2.0512066	0.9941565	Gompertz
Inoculum (%)	**3**	**1.5704463**	**0.7214560**	**−0.2961272**	**0.9968111**	**1.6087664**	**0.7136665**	**−0.3830667**	**0.9906419**	**Logistic**
	5	1.6966200	0.6240038	−0.6977070	0.9877158	1.7378880	0.6498374	−0.7140678	0.9792428	Logistic
	7	1.7062470	0.6242161	−0.9487466	0.9977497	1.7322425	0.6932986	−0.8616368	0.9955105	Logistic
	10	1.727970	0.558232	−1.332860	0.9794106	1.7477825	0.6454246	−1.1578794	0.9730414	Logistic
Chlorpyrifos (mg L^{-1})	100	0.5725116	0.1107258	−1.1095735	0.9921185	0.6633015	0.1065190	−1.2450194	0.9889417	Logistic
	200	0.5665512	0.1116399	−1.4877092	0.9959021	0.6227163	0.1118637	−1.5264380	0.9924068	Logistic
	300	0.5422157	0.1396415	−0.8967360	0.997702	0.5776322	0.1409734	−0.9369330	0.9953714	Logistic
	400	0.5727369	0.1346653	−1.2800365	0.9903011	0.6010975	0.1427138	−1.2116374	0.9924553	Gompertz
	500	0.6533903	0.2543835	−0.5458178	0.9496665	0.6742996	0.2664076	−0.5279734	0.9662146	Gompertz
	600	**0.8633592**	**0.2787160**	**−0.4444979**	**0.9783295**	**0.8981414**	**0.2890873**	**−0.4565587**	**0.9879685**	**Gompertz**
	700	0.8432418	0.2573163	−0.3556326	0.9890925	0.9195100	0.2394345	−0.5373703	0.977839	Logistic
	800	0.8320603	0.2170250	−0.2239014	0.9863982	0.9956559	0.1941392	−0.4725107	0.976922	Logistic
	900	0.6227636	0.1557790	−0.6373144	0.99274	0.6977168	0.1470682	−0.8020819	0.9854815	Logistic
	1000	0.3204507	0.1012620	−1.5247021	0.9999403	0.3235203	0.1208006	−1.2789039	0.9994088	Logistic
Temperature (°C)	5	0.80179920	0.02911697	−33.10521679	0.9678422	0.80241916	0.04120519	−27.40216944	0.9678958	Gompertz
	20	1.9665463	0.3103073	−2.5874650	0.9818219	2.0774736	0.3387348	−2.3468771	0.9855865	Gompertz
	28	**2.215580**	**0.436109**	**−1.780004**	**0.9917402**	**2.3439810**	**0.4644297**	**−1.6669626**	**0.992993**	**Gompertz**
	37	2.4568257	0.3677034	−2.0023596	0.9619962	2.8835480	0.3602088	−2.0979157	0.958767	Logistic

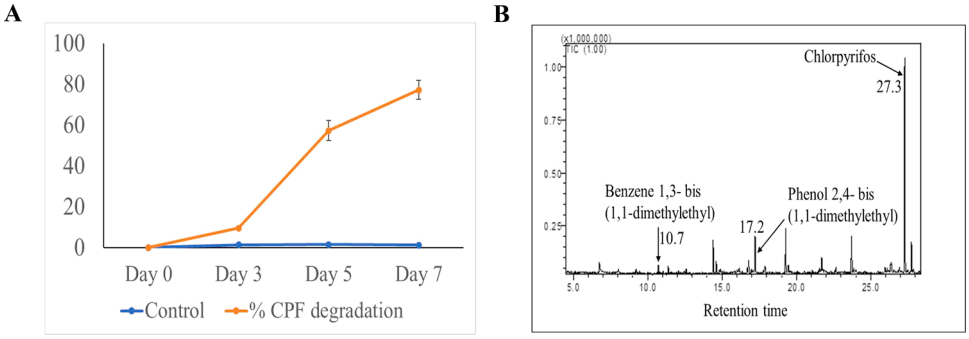

Fig. 2. GC–MS data showing chlorpyrifos degradation and metabolite profiling by strain ISTPL4. (A) Percent degradation of chlorpyrifos (600 mg L^{-1}) under optimized conditions. Residual CPF concentration was monitored over 7 days, with abiotic control showing negligible degradation. **(B)** GC–MS chromatogram showing the presence of metabolites benzene, 1,3-bis (1,1-dimethyl ethyl) and phenol, 2,4-bis (1,1-dimethyl ethyl) in the day 7 sample.

Table 2
Previous reports on chlorpyrifos degradation by different bacterial genera.

Bacterial strain	CPF concentration (mg L^{-1})	Degradation time	Degradation (%)	References
Sphingobacterium sp. C1B	42	14 d	–	Verma et al. (2020)
Shewanella sp. BT05	50	24 h	80.5	Govarthanan et al. (2020)
Pseudomonas sp. CB2	100	5 d	74.6	Zhang et al. (2018)
Ochrobactrum sp. CPD-03	100	48 h	85–88	Nayak et al. (2020)
Bacillus cereus PM38	300	48 h	98.4	Pakar et al. (2024)
Klebsiella pneumoniae CP19	300	14 d	85.4	Elshikh et al. (2022)
Zhihengliuella sp. ISTPL4	600	7 d	76.95	This study

CPF: chlorpyrifos.

both metabolites decreased in day 5 and day 7 samples, indicating their further transformation **(Supplementary Fig. S9).** The temporal variation in metabolite peak intensity, with an initial increase followed by a decrease, further supports their role as transient degradation intermediates. TCP was not detected during the 7-day biodegradation process. Fig. 3 illustrates the proposed CPF degradation pathway by

Table 3
GC-MS identified metabolites formed during chlorpyrifos degradation by strain ISTPL4.

No.	Metabolite	Retention time (min)	0 d	3 d	5 d	7 d
1	Chlorpyrifos	27.3	+	+	+	+
2	Benzene, 1,3-bis(1,1-dimethylethyl)	10.7	–	+	+	+
3	Phenol, 2,4-bis(1,1-dimethylethyl)	17.2	–	+	+	+

"+" indicates presence; "–" indicates absence of the compound.

strain ISTPL4 based on the identified metabolites. These findings, together with the observed increase in biomass (OD_{600}), confirm that CPF was actively metabolized and utilized by strain ISTPL4 rather than merely tolerated.

3.4. Estimation of chloride ion concentration

The concentration of Cl^- ions was assessed using the Mohr titration method with dilute K_2CrO_4 as the indicator. The potential reactions occurring during titration are represented below (Wulandari et al., 2025):

$$NaCl\ (aq) + AgNO_3\ (aq) \rightarrow AgCl\ (s) + NaNO_3\ (aq)$$

$$2\ AgNO_3\ (aq) + K_2CrO_4\ (aq) \rightarrow Ag_2CrO_4\ (s) + 2\ KNO_3\ (aq)$$

Initially, a white silver chloride precipitate was formed, as described in the first reaction. The endpoint of the titration was indicated by the appearance of a brick-red precipitate of silver chromate. $AgNO_3$ was standardized prior to use as the titrant. NaCl solution was used as the primary standard because of its high purity, stability, and resistance to oxidation. The concentrations of Cl^- ions measured on days 3, 5, and 7 were 40.9, 91.88, and 145.85 mg L^{-1}, respectively.

3.5. In silico analysis

3.5.1. Retrieval of protein primary sequences

Whole genome sequencing of strain ISTPL4 (NCBI BioProject ID: PRJNA421074 with GenBank accession number: CP025422.1) revealed the presence of several esterase enzymes that might be involved in the CPF degradation (Mishra et al., 2018). The FASTA sequences of five esterase enzymes, namely carboxylesterase B, carboxylesterase NlhH, esterase YbfF, phosphotriesterase, and acetylxylan esterase, with accession numbers WP_199,399,158, WP_101,847,418, WP_101,844,417, WP_101,848,176, and WP_101,847,773, respectively, were retrieved from the National Center for Biotechnology Information (NCBI) database (http://www.ncbi.nlm.nih.gov/).

3.5.2. Physicochemical characterization

The physicochemical characteristics of five proteins were analyzed with the help of Expasy's ProtParam tool. The results of the ProtParam analysis are summarized in **Supplementary Table S1.** The molecular weights of carboxylesterase B, carboxylesterase NlhH, esterase YbfF, phosphotriesterase, and acetylxylan esterase were computed to be 55, 30, 27, 35, and 27 kDa, respectively. The theoretical pI values for carboxylesterase B, carboxylesterase NlhH, esterase YbfF, phosphotriesterase, and acetylxylan esterase were 4.12, 4.46, 6.16, 5.33, and 5.43, respectively. The instability index values for carboxylesterase B, carboxylesterase NlhH, esterase YbfF, phosphotriesterase, and acetylxylan esterase were 34.86, 35.48, 34.42, 24.44, and 34.52, respectively. The corresponding aliphatic index values were 81.64, 83.16, 91.11, 91.27, and 101.96 respectively. In addition, GRAVY values for carboxylesterase B, carboxylesterase NlhH, esterase YbfF, phosphotriesterase, and acetylxylan esterase were −0.150, −0.041, −0.196, −0.101, and −0.008 respectively.

3.5.3. Secondary structure prediction

Secondary structural features predicted using SOPMA are listed in **Supplementary Table S2.** Random coils were found to predominate over α-helices in esterase YbfF, carboxylesterase NlhH, and

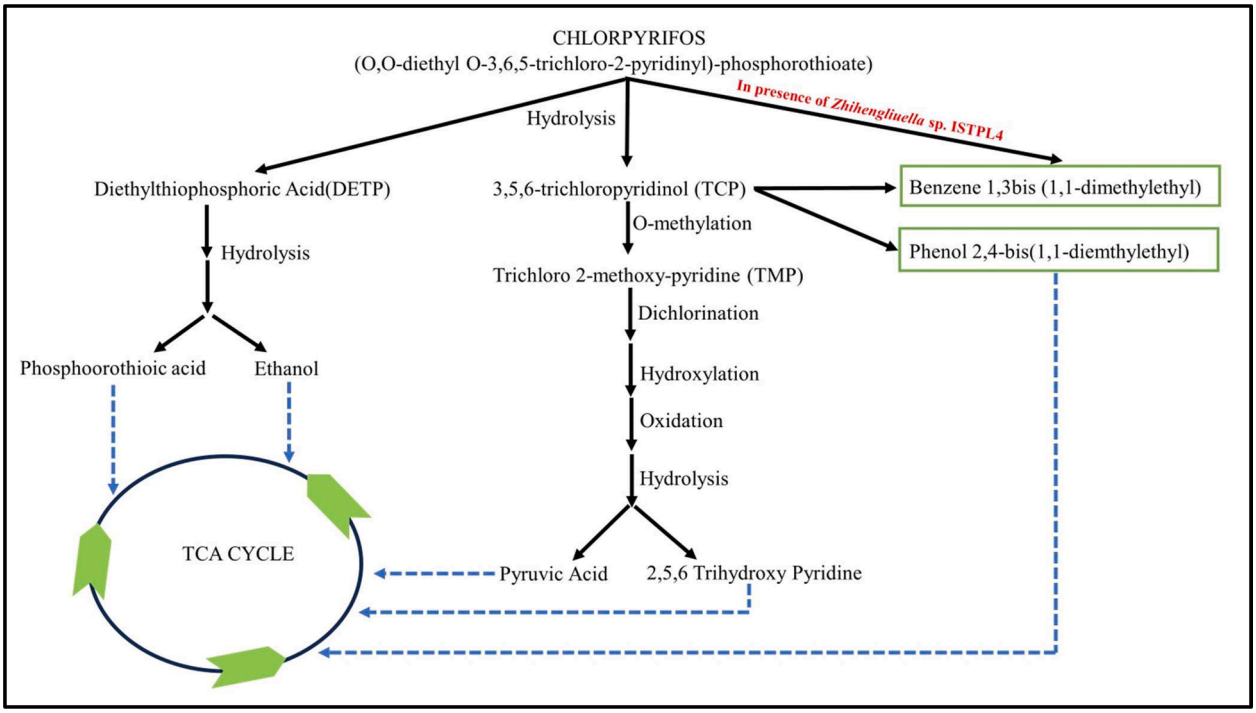

Fig. 3. Possible degradation pathway of chlorpyrifos. In the presence of *Zhihengliuella* sp. ISTPL4, chlorpyrifos forms benzene, 1,3-bis (1,1-dimethyl ethyl) and phenol, 2,4-bis (1,1-dimethyl ethyl) without the formation of TCP and DETP.

phosphotriesterase, followed by extended strands and ß-turns. In contrast, α-helices predominated over random coils in carboxylesterase B and acetylxylan esterase, followed by extended strands and ß-turns.

3.5.4. Phylogenetic tree analysis

Phylogenetic analysis revealed the presence of two major clusters, with proteins belonging to the same enzyme family grouped together, including acetylxylan esterase, carboxylesterase B, phosphotriesterase, esterase YbfF, and carboxylesterase NlhH **(Supplementary Fig. S10)**. For acetylxylan esterase, the minimum degree of divergence was observed among *Microbacterium* sp. strain K36, strain China, and *Microbacterium paraoxydans,* whereas the maximum divergence was observed between *Zhihengliuella* sp. ISTPL4 and *Microbacterium* sp. Nx66. For carboxylesterase B, the minimum degree of divergence was observed between *Zhihengliuella* sp. ISTPL4 and *Microbacterium paraoxydans*, while the maximum divergence was observed between *Zhihengliuella* sp. ISTPL4 and *Microbacterium* sp. NPDC091676. In the case of phosphotriesterase, the minimum divergence was observed between *Zhihengliuella* sp. ISTPL4 and *Microbacterium paraoxydans* as well as *Microbacterium* sp. GbtcB4. The maximum divergence was observed between *Zhihengliuella* sp. ISTPL4 and both *Microbacterium* sp. Y-01 and *Microbacterium algeriense*. For esterase YbfF, the minimum degree of divergence was observed between *Zhihengliuella* sp. ISTPL4 and *Microbacterium* sp. Nx66, whereas the maximum divergence was observed between *Zhihengliuella* sp. ISTPL4 and *Microbacterium* sp. NPDC055988. Similarly, the minimum degree of divergence for carboxylesterase NlhH was observed between *Zhihengliuella* sp. ISTPL4 and *Microbacterium* sp. Y-01 as well as *Microbacterium algeriense*, while the maximum divergence was observed between *Zhihengliuella* sp. ISTPL4 and *Microbacterium* sp. KSW4–4. Overall, the phylogenetic analysis suggested that these genes evolved from a common ancestral origin.

3.5.5. Three-dimensional modeling of receptor molecules

3D structures of the five receptor proteins were predicted using templates generated through ColabFold. Ramachandran plot analysis was used to identify energetically favorable regions within the protein structures. These results indicated that the predicted 3D structures were reliable and suitable for further enzymatic and structural analyses. Additionally, the reliability of each structural model was evaluated using the mean predicted local distance difference test (pLDDT) score generated by ColabFold. **Supplementary Table S3** presents the top five template hits ranked according to E-value and bit score from the pdb70. m8 output file.

3.5.5.1. Esterase YbfF. The predicted structural models of esterase YbfF showed stable inter-residue distance matrices and uniformly low predicted aligned error (PAE) values. The pLDDT scores exceeded 90 for most residues, indicating high confidence in the predicted structure. Slightly lower scores were observed in the central region, possibly due to lower multiple sequence alignment (MSA) coverage. The pLDDT plots of all five esterase enzymes are presented in **Supplementary Fig. S11.** MolProbity validation of the YbfF model yielded a clashscore of 2.03, with 96.8% of residues located within favored Ramachandran regions.

3.5.5.2. Carboxylesterase B. The structural models of carboxylesterase B demonstrated consistent topology and moderately high pLDDT scores across all predictions. MolProbity validation showed a clash score of 1.6, with 96.85% of residues located within favored Ramachandran regions and 97.89% favored rotamers. Moreover, bond lengths were close to ideal values, resulting in an overall MolProbity score of 1.10.

3.5.5.3. Carboxylesterase NlhH. The predicted model of NlhH showcased robust structural features supported by high pLDDT values throughout the sequence. Minor reductions in confidence were observed in some regions, possibly indicating flexible loop or terminal regions. MolProbity validation reported a score of 1.03 with a low clash score of 1.72, while 97% of residues were present within favored Ramachandran regions.

3.5.5.4. Acetylxylan esterase. This enzyme exhibited a well-folded core domain characterized by high pLDDT scores and low PAE values. The validated structure showcased a clash score of 1.62 and a MolProbity score of 1.19, with no Ramachandran or rotamer outliers. Furthermore, >95% of residues and side chains were present in favored conformations.

3.5.5.5. Phosphotriesterase homology protein. The predicted phosphotriesterase structure exhibited a compact global fold with high pLDDT values across most of the sequence. Minor decreases in confidence were observed around residues 100–110, 140, and 270 within the MSA. The all-atom clash score was 3.76, indicating minimal steric clashes. MolProbity analysis yielded a score of 1.21, with minimal bond angle outliers, one Ramachandran outlier, and 97% of residues located within favored Ramachandran regions.

Overall, the protein modeling results indicated highly accurate backbone predictions, providing a reliable structural foundation for further analysis, including functional annotation, mutagenesis design, and molecular docking studies.

3.6. Molecular docking studies

To evaluate the binding potential of the candidate enzymes, CPF was docked with five proteins, namely carboxylesterase B, carboxylesterase NlhH, esterase YbfF, phosphotriesterase, and acetylxylan esterase. The best docking conformation for each protein-ligand complex was selected based on binding affinity and RMSD values. CPF exhibited favorable binding interactions with all five proteins.

Among the enzymes evaluated, acetylxylan esterase exhibited a moderate binding affinity of −4.4 kcal mol^{-1}. CPF was stabilized through conventional hydrogen bonding with THR222 and hydrophobic interactions involving ALA20, LEU23, and GLY220. Carboxylesterase NlhH showed a slightly lower binding affinity of –4.1 kcal mol^{-1}, with interactions involving ASP172 and GLU171 through van der Waals and pi-anion interactions. Esterase YbfF showed a binding affinity of –5 kcal mol^{-1}, with CPF stabilized through van der Waals, pi-pi T-shaped, and pi-alkyl interactions involving residues such as HIS233, HIS91, and GLN133. Similarly, phosphotriesterase exhibited a binding affinity of –5 kcal mol^{-1}, with CPF forming hydrogen bonds with ARG216 and ARG240, along with additional stabilizing interactions including pi-anion interactions and hydrogen bonding. These results suggest that multiple enzymes are capable of accommodating CPF within their binding pockets.

Carboxylesterase B demonstrated the strongest binding affinity (–5.7 kcal mol^{-1}), indicating the higher binding stability compared to the other enzymes. The best docking pose (mode 1) showed an RMSD of 0.000 Å, indicating a highly stable conformation. Structural visualization revealed that CPF was well accommodated within the predicted binding pocket, forming a network of van der Waals (ASN391, GLY270, THR407), π-alkyl and alkyl (TYR395, VAL269, TRP422), and π-sulfur (PHE387) interactions, suggesting a favorable binding environment.

Representative docking interactions between CPF and carboxylesterase B are shown in Fig. 4, including both the 3D binding pose and 2D interaction diagram. Complete docking results for all five enzymes, including binding affinities and interaction residues, are provided in **Supplementary Table S4**, while the corresponding visualizations are presented in **Supplementary Fig. S12**. Docking analyses and visualizations were performed using PyMOL and BIOVIA Discovery Studio Visualizer. Based on its stronger binding affinity and stable interaction profile, the carboxylesterase B-CPF complex was selected for further MD simulations to evaluate structural stability and dynamic behavior.

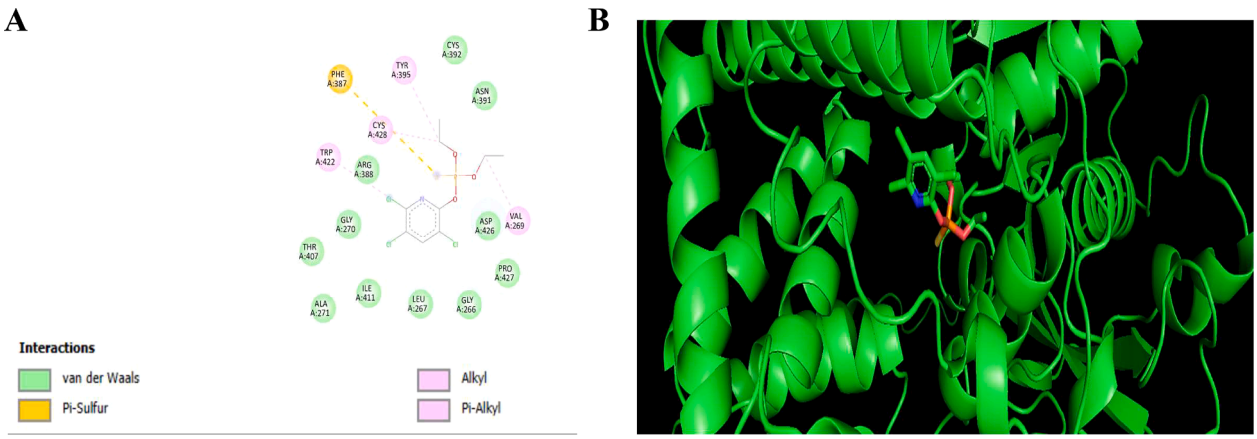

Fig. 4. Docking interaction of chlorpyrifos with carboxylesterase B. (A) 3D binding pose and **(B)** 2D interaction diagram highlighting key interacting residues.

3.7. Molecular dynamics simulation

3.7.1. Trajectory analysis

The RMSD plot of the Cα atoms provides insight into the structural stability and convergence behavior of the carboxylesterase B receptor (black trace) and CPF ligand (red trace) throughout the simulation period (Fig. 5**A**). The RMSD of carboxylesterase B increased sharply during the initial stage (0–10 ns), reflecting significant conformational changes as the system relaxed and adapted to the simulation environment. This initial increase reflects the transition from the starting structure to a more energetically favourable conformation. Between 10 and 50 ns, RMSD values fluctuated around 0.3 nm, reflecting transient structural rearrangements. After 60 ns, the receptor stabilizes, reflecting a relatively equilibrated state with little structural deviation. In contrast CPF showed remarkable stability with consistent RMSD values around 0.1 nm, indicating minimal conformational change and high binding stability. This difference reflects the dynamic nature of the receptor compared to the rigid ligand structure.

The RMSF plot revealed higher fluctuations in certain regions, particularly residues 100–200 and 400–500, indicating greater flexibility within these segments. These peaks likely correspond to loop regions or less structured parts of the protein. In contrast, most residues, especially in the central region of the protein, showed relatively low RMSF values, suggesting stable and well-structured domains (Fig. 5**B**).

To evaluate whether the observed stability was ligand-specific, a 50 ns MD simulation of the apo form of carboxylesterase B was also performed. The RMSD profile of the apo-enzyme demonstrated stable behavior throughout the simulation, indicating that the protein possesses inherent structural stability. The RMSD plot of the apo protein is presented in the **Supplementary Fig. S13**. Both apo and CPF-bound systems exhibited stable RMSD profiles, indicating that the overall structural stability is largely an intrinsic property of the enzyme.

3.7.2. Temporal distribution

The temporal evolution of structural clusters for the carboxylesterase B–CPF complex during the 100 ns simulation is presented in **Supplementary Fig. S14**. Blue dots represent sampled clusters throughout the simulation trajectory, whereas the red line indicates average cluster index over time. During the first stage (0–20 ns), high cluster variability was observed, suggesting high conformational changes as the system adapted to the simulation environment. Between 20 and 50 ns, frequent switching between clusters suggested structural dynamic changes. At 60 ns, the cluster pattern stabilizes with reduced transitions and a major cluster exhibited stability for large times. This stabilization indicates equilibration of the receptor-ligand complex with minimal large-scale conformational changes. The time-averaged cluster index showed fluctuating behavior during the early simulation stages but stabilized during the later stages, supporting structural convergence.

The presence of multiple clusters initially reflects structural adaptation, while the reduction to fewer clusters at later stages indicates system stabilization. These results align with the RMSD trends, confirming extensive structural exploration before stabilization.

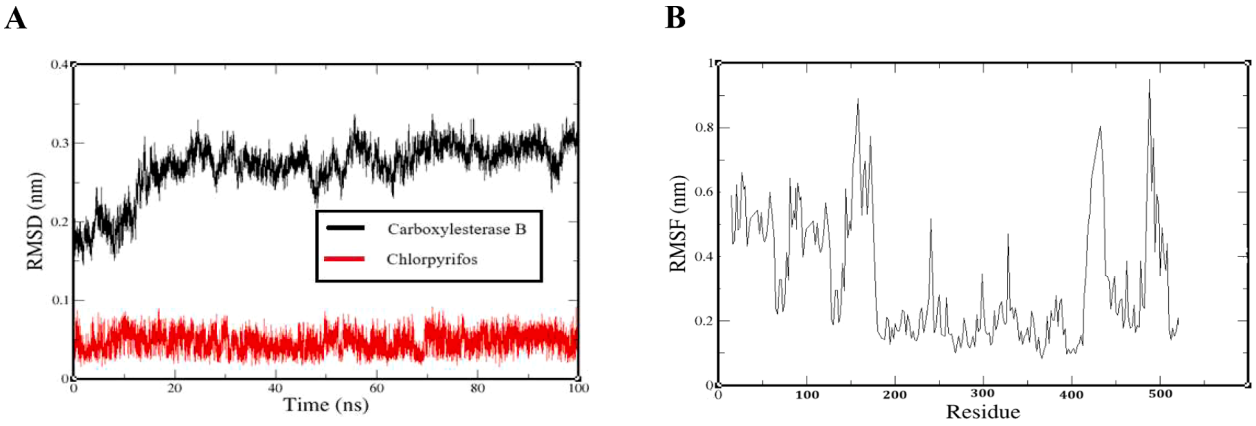

Fig. 5. RMSD and RMSF plot of carboxylesterase B receptor and chlorpyrifos pesticide. (A) RMSD plot of the structural stability of the carboxylesterase B receptor (black line) and the chlorpyrifos pesticide (red line). The receptors first experience a conformational change before stabilizing at approximately 0.3 nm, while the pesticide is very stable with little fluctuation at 0.1 nm, reflecting strong binding stability in the system, **(B)** Root Mean Square Fluctuation (RMSF) plot depicting residue-wise flexibility of the protein throughout the simulation. Higher RMSF values around residues 100–200 and 400–500 indicate flexible regions, likely corresponding to loops, while lower values in other regions suggest more stable and structured domains.

3.7.3. Solvent accessible surface area (SASA)

SASA profile of the carboxylesterase B-CPF complex over the 100 ns simulation time is shown in **Supplementary Fig. S15**. The black trace represents the raw SASA fluctuations of the receptor in the presence of CPF, whereas the red line marks the time-averaged SASA values throughout the simulation. The SASA values ranged approximately between 115 nm^2 and 140 nm^2 with a general decreasing trend, implying conformation changes in the presence of the ligand. A notable reduction in SASA was seen around 20 ns, which may be attributed to initial structural realignment. Between 40 ns to 80 ns, the SASA values remained stable with intermittent fluctuations, indicative of dynamic equilibrium in the complex of the receptor and ligand**.** The red line (averaged SASA) reduces these oscillations, showing a general decreasing trend.

3.7.4. Hydrogen bond analysis

Supplementary Fig. S16 illustrates the variation in hydrogen bonding interactions between carboxylesterase B and CPF during the 100 ns (100,000 ps) simulation. The black line represents the instantaneous count of hydrogen bonds, while the red line illustrates the time-averaged trend. The number of hydrogen bonds fluctuated between 0 and 5, illustrating intricate interactions between the receptor and ligand. For most of the simulation, 1–2 hydrogen bonds were consistently maintained, indicating occasional but continued hydrogen bonding. A temporary increase to up to 5 hydrogen bonds was observed between 40,000 and 60,000 ps, suggesting stronger interactions during this period.

3.7.5. Principal component analysis (PCA)

PCA of the carboxylesterase B–CPF complex over the 100 ns revealed four distinct principal components, with Vector 1 representing the dominant core motion. Vector 1 exhibited high initial amplitudes (approximately 5 units) that progressively decreased to nearly 0 units after 40 ns, indicating substantial early structural rearrangement followed by stabilization. This trend suggests that Vector 1 captures the essential dynamics associated with ligand binding. The corresponding path visualization highlights the spatial distribution of these conformational changes.

Ribbon representations revealed thickness variations along the backbone, where thicker regions, particularly within peripheral loops and certain secondary structures, corresponded to higher flexibility during the early high-amplitude phase. In contrast, thinner core regions remained comparatively stable over conformational changes **(Supplementary Fig. S17).**

The subsequent main components (Vectors 2–4) represented weaker and more localized motions. Vector 2 showed a transient peak (about 5 units) around 20 ns before declining, suggesting secondary conformational changes. Vectors 3 and 4 displayed low-amplitude fluctuations (–2 to 4 units and ±2 units), showing smaller-scale motions throughout the simulation. Overall, Vector 1 remained the primary contributor to the biological dynamics of the CPF-bounded state.

3.7.6. Free energy calculation

The free energy profile of CPF binding was calculated to measure the thermodynamic favorability of the interaction and to identify the major energetic contributions stabilizing the complex. **Supplementary Table S5** collates the energy components derived through MM-PBSA calculations in kJ/mol with their respective standard deviations.

The overall binding free energy of CPF was –697.49 ± 39.96 kJ/mol, showing strong and spontaneous interaction between the CPF and the enzyme. Van der Waals interactions represented the most stabilizing factor (–483.82 ± 17.19 kJ/mol), indicating the importance of hydrophobic contacts and shape complementarity within the binding pocket. The tight non-polar packing of the ligand in the active site seems to be a pre-eminent stabilizing factor. Electrostatic interactions also contributed significantly to binding stability (–122.43 ± 7.93 kJ/mol), likely arising from favorable charge and dipole–dipole interactions with residues such as ARG, HIS, and GLN.

In contrast, polar solvation energy opposed binding (+147.26 ± 32.13 kJ/mol), reflecting the stabilization of the unbound (solvated) states in solution. This destabilization effect was negated by SASA energy contribution of –238.50 ± 0.28 kJ/mol. This term captures beneficial desolvation and hydrophobic burial effects that reinforce binding stability by minimizing solvent exposure of non-polar ligand surfaces.

3.8. Caeb gene amplification

The carboxylesterase B (*Caeb*) gene was amplified and visualized at approximately 1500 base pairs against a 1 kb DNA ladder (**Supplementary Fig. S18**). This gene was selected for amplification based on the *in-silico* analyses, which indicated the strongest affinity towards CPF among the analyzed enzymes. The amplified product size was consistent with the expected gene length of 1554 base pairs.

4. Discussion

The present study provides a comprehensive evidence that *Zhihengliuella* sp. ISTPL4 possesses significant potential for CPF biodegradation. By integrating physiological optimization, GC–MS metabolite profiling, dechlorination assay, molecular docking, MD simulations, and free energy calculations, this study establishes a multi-level understanding of CPF detoxification by strain ISTPL4.

Initial screening revealed that strain ISTPL4 preferentially utilized CPF over malathion, monocrotophos, and dimethoate, suggesting substrate specificity towards compounds containing phosphoester bonds. The ability of strain ISTPL4 to grow in MSM supplemented solely with CPF indicates that the pesticide serves as a carbon and energy source rather than mere co-metabolic transformation, which is important for bioremediation in nutrient-limited soils.

Optimization studies further revealed that maximum degradation occurred at 28 °C and pH 5 with a 3% inoculum size, while the strain tolerated salinity levels up to 7%. Such tolerance suggests ecological adaptability and supports its application in diverse soil conditions, including mildly saline and acidic agricultural fields. The highest growth rate observed at 600 mg L^{-1} CPF further indicates that strain ISTPL4 can withstand and metabolize relatively high pesticide concentrations, an important feature for the remediation of contaminated sites.

The growth kinetics derived from Logistic and Gompertz models provided further insight into CPF utilization by strain ISTPL4. The higher maximum specific growth rate (μ) observed under optimized conditions indicates enhanced microbial activity during the exponential growth phase. Notably, the increased μ values at 600 mg L^{-1} CPF and pH 5 suggest that CPF utilization is closely associated with active microbial growth, indicating its role as a carbon and energy source. The estimated lag phase (λ) may reflect the adaptation behavior of the strain under CPF stress, where shorter lag phases under favorable conditions suggest quicker acclimatization. The asymptote (A), representing the maximum biomass, provides insight into the carrying capacity of the system under varying environmental conditions. Together, these parameters support the interpretation that CPF utilization by strain ISTPL4 is closely linked to growth dynamics and physiological adaptation under optimized conditions. Although bacterial growth reflects CPF utilization because CPF was provided as the sole carbon and energy source, growth measurements alone may not fully represent the extent of degradation. Therefore, GC–MS was performed under optimized conditions to directly assess CPF degradation, whereas growth-based measurements were used primarily for preliminary optimization studies.

GC–MS analysis confirmed 76.95% degradation of 600 mg L^{-1} CPF within 7 days by strain ISTPL4. TCP has been widely reported as a major intermediate during CPF degradation by other bacterial strains (Haque et al., 2022). In the present study, two intermediates, namely benzene, 1, 3-bis(1,1-dimethylethyl) and phenol, 2,4-bis(1,1-dimethylethyl), were

detected, whereas the commonly reported TCP intermediate was not observed. Additionally, several other metabolites commonly reported during CPF degradation, including 2,5,6-trihydroxy pyridine, diethyl thiophosphate, and chlorpyrifos oxon, were also not detected in this study (Ambreen and Yasmin, 2021). Interestingly, degradation of CPF and TCP by *Sphingobacterium* sp. JAS3 has previously been reported to produce benzene, 1,3-bis(1,1-dimethylethyl) as an intermediate (Abraham and Silambarasan, 2013). Based on earlier reports, phenol, 2, 4-bis(1,1-dimethylethyl) may arise from TCP or diethyl phosphorothioate alkylation reactions and may undergo transformation to pyruvic acid (Das and Yogalakshmi, 2022; Tejashwini et al., 2026).

The detection of these metabolites suggests their involvement in CPF degradation and possible downstream mineralization processes (Yadav et al., 2024). This observation may indicate that any transient TCP formed during degradation is rapidly transformed before accumulation, although limitations associated with detection sensitivity cannot be excluded. Given that TCP is known to persist in soil with a relatively long half-life (65–365 days) (Figueroa-Careaga et al., 2026), its absence in the detected metabolites may reflect efficient transformation pathways in strain ISTPL4.

Several studies have reported pathways in which bacterial strains simultaneously degrade CPF and TCP. For example, in *Micrococcus luteus* ML, CPF is first hydrolyzed to TCP, which is subsequently converted into 2-pyridinol and further degraded (Yue et al., 2023). The observed decrease in metabolite concentrations over 7 days suggests continued transformation and utilization of CPF by strain ISTPL4 as a carbon and energy source.

The dechlorination assay provided additional biochemical evidence of CPF breakdown, as chloride ion concentrations increased progressively over time. Release of inorganic chloride ions confirms cleavage of carbon-chlorine bonds and supports mineralization rather than partial transformation of CPF. TCP degradation requires removal of the three chlorine atoms present on the pyridinol ring followed by ring cleavage. The released chlorine atoms are toxic and may induce oxidative stress that overwhelms bacterial antioxidant systems (Sultana et al., 2022). The correlation between CPF degradation and chloride accumulation further supports the detoxification capability of this strain. Although maximum degradation was observed at pH 5, chloride ion estimation was performed under neutral pH conditions because the Mohr titration method requires near-neutral conditions for accurate endpoint detection. Under acidic conditions, the chromate indicator becomes unreliable, resulting in inaccurate endpoint determination (Susi and Hakim, 2022). The observed increase in chloride ion concentration at pH 7 indicates that dechlorination occurs under these conditions, although degradation efficiency may vary with pH.

Physicochemical characterization of all five proteins showed high structural stability, and the obtained values were consistent with previous studies (Oyewusi et al., 2022). The pI values of all target proteins were below 7, indicating their acidic nature. The greater number of negatively charged residues relative to positively charged residues suggests that these proteins are likely intracellular. In addition, all five proteins exhibited instability index values below 40, indicating structural stability. The proteins also showed high aliphatic index values, suggesting stability across a broad temperature range. Generally, higher aliphatic index values are associated with greater thermostability. Furthermore, the negative GRAVY values observed for all proteins indicate enhanced protein-water interactions due to increased surface hydrophilicity. Secondary structure analysis indicated that all five proteins contained fewer extended strands and β-turns. The α-helical regions were likely stabilized through hydrogen bonding between backbone amide groups, which helps preserve its helical shape and enhances overall protein stability and function. These properties are consistent with proteins functioning in soil ecosystems, where environmental conditions such as temperature and moisture frequently fluctuate.

Molecular docking analysis showed that CPF binds favorably to all five esterases, with carboxylesterase B exhibiting the strong binding affinity. The observed binding energies are consistent with previous reports (Lee et al., 2021; Oyewusi et al., 2022). Esterases typically possess a conserved catalytic triad comprising serine, histidine, and an acidic residue (Asp/Glu), which plays a central role in ester bond hydrolysis. Previous studies on CPF-hydrolyzing esterases have reported the presence of this catalytic triad along with a conserved Gly-X-Ser-X-Gly motif essential for catalytic activity (Wang et al., 2020). Sequence analysis of carboxylesterase B in the present study identified serine, histidine, and acidic residues consistent with the catalytic triad characteristic of esterase enzymes, supporting its potential role in CPF hydrolysis. Furthermore, sequence alignment with a representative bacterial α/β hydrolase (WP_003975294.1) revealed moderate similarity, including conserved glycine-rich regions and functionally relevant residues, suggesting conservation of catalytic features despite overall sequence divergence. Although docking scores alone cannot confirm catalytic turnover, they provide valuable insight into ligand-binding plausibility and active-site compatibility. The docking poses indicated that CPF was positioned within the predicted active site region of carboxylesterase B, suggesting a potentially favorable orientation relative to catalytic residues. These findings are consistent with previous studies implicating esterases as key mediators of OP hydrolysis (Bhende et al., 2022). For instance, a carboxylesterase (EstC) from *Streptomyces lividans* TK24 has been shown to effectively hydrolyze CPF through a catalytic triad-mediated mechanism (Wang et al., 2020). Collectively, these observations support the potential involvement of esterase enzymes in CPF degradation. However, further experimental validation through enzyme assays and gene-level studies is required to confirm their functional role in CPF biodegradation.

To further asses the stability and dynamic behavior of the carboxylesterase B–CPF complex beyond docking analysis, MD simulations were performed. RMSD analysis highlighted the dynamic nature of the protein and confirmed that the system reached convergence during the latter stages of the simulation (Choi et al., 2022). The presence of distinct RMSD profiles for the receptor and ligand suggests that different components of the system exhibit varying degrees of flexibility and stability (Rodriguez et al., 2022). The RMSD profile revealed initial conformational adjustments followed by stabilization after approximately 60 ns, indicating system equilibration. The relatively low RMSD of the ligand (approximately 0.1 nm) suggests stable retention within the active site throughout the simulation. The apo-enzyme also showed stable RMSD behavior, suggesting that the overall structural stability is an intrinsic feature of the protein. However, the stable ligand RMSD and interactions indicate that CPF forms a stable enzyme-ligand complex rather than non-specific stabilization. RMSF analysis showed localized flexibility primarily within loop regions, whereas the catalytic domain remained structurally stable. This balance between flexibility and rigidity is characteristic of catalytically active enzymes that undergo induced-fit conformational adaptation during substrate binding.

Further structural insights were obtained through SASA and radius of gyration analyses, which showed that CPF binding causes receptor compaction and diminished solvent accessibility, implying possible effects on receptor flexibility and function upon ligand binding (Xu et al., 2025). Such compaction may reflect stabilization of the enzyme–substrate complex. Hydrogen bond analysis revealed consistent formation of 1–2 hydrogen bonds, with occasional peaks up to 5 bonds, indicating transient strengthening of ligand interactions. PCA demonstrated dominant early conformational motions followed by convergence, reinforcing notion of dynamic stabilization (Li and Ma, 2025). PCA also provided insight into the spatial distribution of conformational changes across different regions of the protein structure.

Thermodynamic validation through MM-PBSA calculations further supported stable complex formation, with highly negative total binding free energy (−697.49 kJ/mol). This strong negative energy may partly result from exclusion of the entropic contribution (−TΔS), as entropy calculations are often omitted in MM-PBSA analyses because of their

high computational cost and poor convergence behavior (Wang et al., 2018; Genheden and Ryde, 2015). Consequently, MM/PBSA-derived ΔG values are often overestimated and should be interpreted in a relative rather than absolute sense. Such highly negative values are significantly larger than typical binding free energies reported for enzyme-ligand complexes, which generally fall within the range of tens of kJ mol^{-1}. Previous studies on similar systems have reported binding energies ranging from approximately −10 to −30 kJ mol^{-1} (Bantun et al., 2026).

Van der Waals interactions represented the major stabilizing contribution, emphasizing the importance of hydrophobic complementarity between CPF and the active site. Although polar solvation energy opposed binding, this effect was compensated by favorable electrostatic and SASA energy contributions. Moreover, in comparative binding analyses involving structurally similar ligands within the same protein system, entropy contributions are often assumed to partially cancel out, allowing relative binding affinity comparisons based primarily on enthalpic components (Genheden and Ryde, 2015; Golub et al., 2021). Together, these findings suggest that CPF binding to carboxylesterase B is thermodynamically stable and driven primarily by hydrophobic interactions.

Amplification of the *Caeb* gene provided molecular-level support for the computationally predicted role of carboxylesterase B. This experimental validation bridges the gap between *in-silico* predictions and molecular genetics, reinforcing the likelihood that carboxylesterase B plays a central role in CPF degradation. Confirmation of the gene also opens possibilities for recombinant expression and enzyme immobilization strategies aimed at enhancing degradation efficiency.

The observed degradation efficiency and enzymatic potential of strain ISTPL4 suggest its applicability in wastewater treatment systems contaminated with OPs. The ability of the strain to utilize CPF as a sole carbon source, together with the involvement of esterase enzymes, supports its potential application in bioaugmentation and enzyme-assisted remediation strategies. Similar studies have demonstrated effective microbial removal of CPF from wastewater systems, highlighting the feasibility of such approaches under environmentally relevant conditions (Elzakey et al., 2023). In addition, enzyme-mediated CPF hydrolysis by carboxylesterases has been previously reported (Wang et al., 2020). The psychrotolerant nature of strain ISTPL4 may further support its application in low-temperature wastewater systems. However, further validation under complex wastewater matrices and field-scale conditions is necessary to establish its practical applicability.

5. Conclusion

In conclusion, *Zhihengliuella* sp. ISTPL4 demonstrated strong potential for CPF bioremediation, achieving 76.95% removal within 7 days without detectable accumulation of toxic intermediates. The results indicate efficient detoxification and utilization of CPF as a sole carbon and energy source. Integrated experimental and computational analyses suggest that CPF degradation is associated with esterase-mediated processes, with carboxylesterase B identified as a key candidate enzyme exhibiting strong interaction with CPF. These findings provide mechanistic insight into CPF degradation by actinobacteria. Collectively, the findings suggest that strain ISTPL4 could be effectively applied in bioremediation strategies to reduce the environmental impact of CPF contamination, thereby contributing to more sustainable agricultural and environmental management practices. The degradation efficiency, enzymatic potential, and psychrotolerant nature of the strain further highlight its promise for bioremediation of CPF-contaminated environments, including wastewater systems. Nevertheless, further studies under complex environmental conditions and pilot-scale systems are required to establish its practical applicability.

Funding

This research received no specific grant from any funding agency.

CRediT authorship contribution statement

Himanshi Aggarwal: Writing – original draft, Conceptualization. **Divya Chaudhary:** Writing – review & editing, Methodology. **Taruna Kumari:** Methodology, Investigation, Data curation. **Nischal Pradhan:** Writing – original draft, Software. **Vaibhav Mishra:** Methodology, Investigation, Formal analysis. **Antresh Kumar:** Validation, Supervision. **Anamika Singh:** Validation, Data curation. **Ashutosh Pandey:** Supervision, Methodology. **Navaneet Chaturvedi:** Software, Methodology, Investigation. **Laurent Dufossé:** Writing – review & editing, Validation, Supervision, Funding acquisition. **Arti Mishra:** Writing – review & editing, Supervision, Methodology, Conceptualization. **Naveen Chandra Joshi:** Writing – review & editing, Supervision, Methodology, Conceptualization.

Declaration of competing interest

The authors declare that they have no known competing financial interests or personal relationships that could have appeared to influence the work reported in this paper.

Acknowledgements

The authors are also thankful to AIMT, Amity University, Noida for providing facilities. The authors would like to express their sincere thanks to Dr. Ashwani Kumar Tiwari, School of Environmental Sciences, Jawaharlal Nehru University, New Delhi, India, for providing the facility to perform the dechlorination assay. LD deeply thanks the Conseil Régional de La Réunion and the Conseil Régional de Bretagne for the continuous support of research activities dedicated to technology, microbiology and biotechnology.

Supplementary materials

Supplementary material associated with this article can be found, in the online version, at doi:10.1016/j.hazadv.2026.101239.

Data availability

Data will be made available on request.

References

Abraham, J., Silambarasan, S., 2013. Biodegradation of chlorpyrifos and its hydrolyzing metabolite 3, 5, 6-trichloro-2-pyridinol by *sphingobacterium* sp. JAS3. Process Biochem. 48, 1559–1564. https://doi.org/10.1016/j.procbio.2013.06.034.

Abraham, M.J., Murtola, T., Schulz, R., Páll, S., Smith, J.C., Hess, B., Lindahl, E., 2015. GROMACS: high performance molecular simulations through multi-level parallelism from laptops to supercomputers. SoftwareX 1-2, 19–25. https://doi.org/10.1016/j.softx.2015.06.001.

Ambreen, S., Yasmin, A., 2021. Novel degradation pathways for chlorpyrifos and 3, 5, 6-trichloro-2-pyridinol degradation by bacterial strain *Bacillus thuringiensis* MB497 isolated from agricultural fields of Mianwali, Pakistan. Pestic. Biochem. Physiol. 172, 104750. https://doi.org/10.1016/j.pestbp.2020.104750.

Anomi, E., Emmanuel, S., 2025. Preliminary studies on the effect of seasonal weather variation on the physicochemical properties of water samples collected in some area in Abuja, Nigeria. Chem. Res. Technol. 2, 203–210. https://doi.org/10.22034/chemrestec.2025.532343.1052.

Bantun, F., Chaturvedi, N., Jalal, N.A., Faidah, H., Babalghith, A.O., Aldairi, A.F., Haque, S., Kumar, V., 2026. Molecular dynamics-driven optimization of triterpenoid, amidinium, and flavonoid inhibitors targeting dengue NS2B-NS3 protease. Comput. Biol. Chem. 123, 109013. https://doi.org/10.1016/j.compbiolchem.2026.109013.

Baştürk, E., Tulun, Ş., 2024. Remediation of organophosphate pesticide-contaminated soil using soil washing and advanced oxidation processes. Int. J. Environ. Sci. Technol. 21, 5459–5468. https://doi.org/10.1007/s13762-023-05351-4.

Behera, S., Das, S., 2023. Potential and prospects of actinobacteria in the bioremediation of environmental pollutants: cellular mechanisms and genetic regulations. Microbiol. Res. 273, 127399. https://doi.org/10.1016/j.micres.2023.127399.

Berendsen, H.J.C., Postma, J.P.M., van Gunsteren, W.F., Hermans, J., 1981. Interaction models for water in relation to protein hydration. In: Pullman, B. (Ed.), Intermolecular Forces. Springer, pp. 331–342. https://doi.org/10.1007/978-94-015-7658-1_21.

Bhende, R.S., Jhariya, U., Srivastava, S., Bombaywala, S., Das, S., Dafale, N.A., 2022. Environmental distribution, metabolic fate, and degradation mechanism of chlorpyrifos: recent and future perspectives. Appl. Biochem. Biotechnol. 194, 2301–2335. https://doi.org/10.1007/s12010-021-03713-7.

Bosu, S., Rajamohan, N., Al Salti, S., Rajasimman, M., Das, P., 2024. Biodegradation of chlorpyrifos pollution from contaminated environment-A review on operating variables and mechanism. Environ. Res. 248, 118212. https://doi.org/10.1016/j.envres.2024.118212.

Choi, K.E., Kim, J.M., Rhee, J.E., Park, A.K., Kim, E.J., Yoo, C.K., Kang, N.S., 2022. Molecular dynamics studies on the structural stability prediction of SARS-CoV-2 variants including multiple mutants. Int. J. Mol. Sci. 23, 4956. https://doi.org/10.3390/ijms23094956.

Das, A., Yogalakshmi, K.N., 2022. Amino-functionalized magnetic iron nanoparticles as a carrier for laccase enzyme and its potential to degrade chlorpyrifos in contaminated soil: fate and kinetics. Water, Air, Soil Pollut. 233, 145. https://doi.org/10.1007/s11270-022-05591-z.

Elshikh, M.S., Alarjani, K.M., Huessien, D.S., Elnahas, H.A, Esther, A.R., 2022. Enhanced biodegradation of chlorpyrifos by *Bacillus cereus* CP6 and *Klebsiella pneumoniae* CP19 from municipal waste water. Environ. Res. 205, 112438. https://doi.org/10.1016/j.envres.2021.112438.

Elzakey, E.M., El-Sabbagh, S.M., Eldeen, E.E.S.N., Adss, I.A.A., Nassar, A.M.K., 2023. Bioremediation of chlorpyrifos residues using some indigenous species of bacteria and fungi in wastewater. Environ. Monit. Assess. 195, 779. https://doi.org/10.1007/s10661-023-11341-3.

Figueroa-Careaga, A., Rangel-Mendez, R., Cervantes, F.J., Razo-Flores, E., Ontiveros-Valencia, A., 2026. Microbial communities produced palladium nanoparticles for the degradation of 3, 5, 6-trichloro-2-pyridinol, metabolite of the insecticide Chlorpyrifos. J. Nanopart. Res. 28, 34. https://doi.org/10.1007/s11051-025-06542-5.

Genheden, S., Ryde, U., 2015. The MM/PBSA and MM/GBSA methods to estimate ligand-binding affinities. Expert Opin. Drug Discov. 10, 449–461. https://doi.org/10.1517/17460441.2015.1032936.

Golub, P., Antalik, A., Veis, L., Brabec, J., 2021. Machine learning-assisted selection of active spaces for strongly correlated transition metal systems. J. Chem. Theory Comput. 17, 6053–6072. https://doi.org/10.1021/acs.jctc.1c00235.

Govarthanan, M., Ameen, F., Kamala-Kannan, S., Selvankumar, T., Almansob, A., Alwakeel, S.S., Kim, W., 2020. Rapid biodegradation of chlorpyrifos by plant growth-promoting psychrophilic *shewanella* sp. BT05: an eco-friendly approach to clean up pesticide-contaminated environment. Chemosphere 247, 125948. https://doi.org/10.1016/j.chemosphere.2020.125948.

Greer, J.B., Magnuson, J.T., Hester, K., Giroux, M., Pope, C., Anderson, T., Liu, J., Dang, V., Denslow, N.D., Schlenk, D., 2019. Effects of chlorpyrifos on cholinesterase and serine lipase activities and lipid metabolism in brains of rainbow trout (*Oncorhynchus mykiss*). Toxicol. Sci. 172, 146–154. https://doi.org/10.1093/toxsci/kfz167.

Haque, M.A., Hossain, M.S., Ahmad, I., Akbor, M.A., Rahman, A., Manir, M.S., Patel, H. M., Cho, K.M., 2022. Unveiling chlorpyrifos mineralizing and tomato plant-growth activities of *Enterobacter* sp. strain HSTU-ASh6 using biochemical tests, field experiments, genomics, and in silico analyses. Front. Microbiol. 13, 1060554. https://doi.org/10.3389/fmicb.2022.1060554.

Hess, B., Bekker, H., Berendsen, H.J.C., Fraaije, J G E M, 1997. LINCS: a linear constraint solver for molecular simulations. J. Comput. Chem. 18, 1463–1472. https://doi.org/10.1002/(SICI)1096-987X(199709)18:12<1463::AID−CC4>3.0.CO;2-H.

Huang, Y., Zhang, W., Pang, S., Chen, J., Bhatt, P., Mishra, S., Chen, S., 2021. Insights into the microbial degradation and catalytic mechanisms of chlorpyrifos. Environ. Res. 194, 110660. https://doi.org/10.1016/j.envres.2020.110660.

Humphrey, W., Dalke, A., Schulten, K., 1996. VMD: visual molecular dynamics. J. Mol. Graph. Model 14, 33–38. https://doi.org/10.1016/0263-7855(96)00018-5.

Islam, N., Iyer, R., 2021. Functional analysis of chlorpyrifos biodegradation in agricultural soils augmented with a three-strain bacterial consortium. Water (Basel) Air Soil Pollut. 232, 425. https://doi.org/10.1007/s11270-021-05349-z.

Kiran, M., Sindhu, R., Raju, N.S., Supreeth, M., 2025. Recent advances in biological removal of Chlorpyrifos from the environment. Int. J. Environ. Res. 19, 187. https://doi.org/10.1007/s41742-025-00857-w.

Kumar, G., Lal, S., Soni, S.K., Maurya, S.K., Shukla, P.K., Chaudhary, P., Bhattacherjee, A. K., Garg, N., 2022. Mechanism and kinetics of chlorpyrifos co-metabolism by using environment restoring microbes isolated from rhizosphere of horticultural crops under subtropics. Front. Microbiol. 13, 891870. https://doi.org/10.3389/fmicb.2022.891870.

Kumari, R., Kumar, R., Open Source Drug Discovery Consortium, Lynn, A., 2014. g_mmpbsa A GROMACS tool for high-throughput MM-PBSA calculations. J. Chem. Info. Model. 54, 1951–1962. https://doi.org/10.1021/ci500020m.

Kundu, A., Mishra, S., Vadassery, J., 2018. *Spodoptera litura*-mediated chemical defense is differentially modulated in older and younger systemic leaves of *Solanum lycopersicum*. Planta 248, 981–997. https://doi.org/10.1007/s00425-018-2953-3.

Lee, H.Y., Cho, D.Y., Ahmad, I., Patel, H.M., Kim, M.J., Jung, J.G., Jeong, E.H., Haque, M. A., Cho, K.M., 2021. Mining of a novel esterase (est3S) gene from a cow rumen metagenomic library with organosphosphorus insecticides degrading capability: catalytic insights by site directed mutations, docking, and molecular dynamic simulations. Int. J. Biol. Macromol. 190, 441–455. https://doi.org/10.1016/j.ijbiomac.2021.08.224.

Li, H., Ma, A., 2025. Enhanced sampling of protein conformational changes via true reaction coordinates from energy relaxation. Nat. Commun. 16, 786. https://doi.org/10.1038/s41467-025-55983-y.

Lindahl, E., Abraham, M., Hess, B., van der Spoel, D., GROMACS Development Team, 2021. GROMACS user manual version 2021.4. https://manual.gromacs.org/.

Mali, H., Shah, C., Patel, D.H., Trivedi, U., Subramanian, R.B., 2022. Degradation insight of organophosphate pesticide chlorpyrifos through novel intermediate 2, 6-dihydroxypyridine by *arthrobacter* sp. HM01. Bioresour. Bioprocess. 9, 31. https://doi.org/10.1186/s40643-022-00515-5.

Mirdita, M., Schütze, K., Moriwaki, Y., Heo, L., Ovchinnikov, S., Steinegger, M., 2022. ColabFold: making protein folding accessible to all. Nat. Methods 19, 679–682. https://doi.org/10.1038/s41592-022-01488-1.

Mishra, A., Gupta, B., Kumar, N., Singh, R., Varma, A., Thakur, I.S., 2020a. Synthesis of calcite-based bio-composite biochar for enhanced biosorption and detoxification of chromium Cr (VI) by *Zhihengliuella* sp. ISTPL4. Bioresour. Technol. 307, 123262. https://doi.org/10.1016/j.biortech.2020.123262.

Mishra, A., Jha, G., Thakur, I.S., 2018. Draft genome sequence of *zhihengliuella* sp. strain ISTPL4, a psychrotolerant and halotolerant bacterium isolated from Pangong Lake, India. Genome Announc. 6, 10–1128.0.

Mishra, A., Rathour, R., Singh, R., Kumari, T., Thakur, I.S., 2020. Degradation and detoxification of phenanthrene by actinobacterium *Zhihengliuella* sp. ISTPL4. Environ. Sci. Pollut. Res. Int. 27, 27256–27267. https://doi.org/10.1007/s11356-019-05478-3.

Nandhini, A.R., Harshiny, M., Gummadi, S.N., 2021. Chlorpyrifos in environment and food: a critical review of detection methods and degradation pathways. ESPI 23, 1255–1277. https://doi.org/10.1039/D1EM00178G.

Nandi, N.K., Vyas, A., Akhtar, M.J., Kumar, B., 2022. The growing concern of chlorpyrifos exposures on human and environmental health. Pestic. Biochem. Physiol. 185, 105138. https://doi.org/10.1016/j.pestbp.2022.105138.

Nayak, P., Solanki, H., 2021. Pesticides and Indian agriculture—a review. Int. J. Res. Granthaalayah 9, 250–263.

Nayak, T., Panda, A.N., Kumari, K., Adhya, T.K, Raina, V., 2020. Comparative genomics of a paddy field bacterial isolate *ochrobactrum* sp. CPD-03: analysis of chlorpyrifos degradation potential. Indian J. Microbiol. 60 (3), 325–333. https://doi.org/10.1007/s12088-020-00864-9.

Oyewusi, H.A., Huyop, F., Wahab, R.A., 2022. Molecular docking and molecular dynamics simulation of Bacillus thuringiensis dehalogenase against haloacids, haloacetates and chlorpyrifos. J. Biomol. Struct. Dyn. 40, 1979–1994. https://doi.org/10.1080/07391102.2020.1835727.

Pakar, N.P., Rehman, F.U., Mehmood, S., Ali, S., Zainab, N., Munis, M.F.H, Chaudhary, H.J., 2024. Microbial detoxification of chlorpyrifos, profenofos, monocrotophos, and dimethoate by a multifaceted rhizospheric Bacillus cereus strain PM38 and its potential for the growth promotion in cotton. Environ. Sci. Pollut. Res. 31 (27), 39714–39734. https://doi.org/10.1007/s11356-024-33804-x.

Raffa, C.M., Chiampo, F., 2021. Bioremediation of agricultural soils polluted with pesticides: a review. Bioengineering 8, 92. https://doi.org/10.3390/bioengineering8070092.

Raj, A., Kumar, A., 2022. Recent advances in assessment methods and mechanism of microbe-mediated chlorpyrifos remediation. Environ. Res. 214, 114011. https://doi.org/10.1016/j.envres.2022.114011.

Rodriguez, J.A., Gonzalez, J., Arboleda-Bustos, C.E., Mendoza, N., Martinez, C., Pinzon, A., 2022. Computational modeling of the effect of five mutations on the structure of the ACE2 receptor and their correlation with infectivity and virulence of some emerged variants of SARS-CoV-2 suggests mechanisms of binding affinity dysregulation. Chem. Biol. Interact. 368, 110244. https://doi.org/10.1016/j.cbi.2022.110244.

Rodríguez-Liébana, J.A., Mingorance, M.D., Peña, A., 2018. Thiacloprid adsorption and leaching in soil: effect of the composition of irrigation solutions. Sci. Total Environ. 610-611, 367–376. https://doi.org/10.1016/j.scitotenv.2017.08.028.

Saitou, N., Nei, M., 1987. The neighbor-joining method: a new method for reconstructing phylogenetic trees. Mol. Bio. Evol. 4, 406–425. https://doi.org/10.1093/oxfordjournals.molbev.a040454.

Schrödinger LLC (2020) The PyMOL molecular graphics system, version 2.5.

Sharma, A., Shukla, A., Attri, K., Kumar, M., Kumar, P., Suttee, A., Singh, G., Barnwal, R. P., Singla, N., 2020. Global trends in pesticides: a looming threat and viable alternatives. Ecotoxicol. Environ. Saf. 201, 110812. https://doi.org/10.1016/j.ecoenv.2020.110812.

Sultana, S., Crompton, M.E., Meurer, K., Jankiewicz, O., Morales, G.H., Johnson, C., Horbach, E., Hoffmann, K.P., Kr, P., Shah, R., Anderson, G.M., 2022. Redox-mediated inactivation of the transcriptional repressor RcrR is responsible for uropathogenic *E. coli*'s increased resistance to reactive chlorine species. MBio 13. https://doi.org/10.1128/mbio.01926-22, 01926-22.

Susi, S., Al Hakim, H.M., 2022. Comparison of NaCl levels in seasoning powder formulation of Nagara bean flour (*Vigna unguiculata* ssp. cylindrica) and oyster mushroom using the Mohr method by direct titration and ash mineral titration. J. Appl. Food Technol. (Singap. World Sci.) 9 (2), 24–29. https://doi.org/10.17728/jaft.12547.

Takkar, S., Tyagi, B., Kumar, N., Kumari, T., Iqbal, K., Varma, A., Thakur, I.S., Mishra, A., 2022. Biodegradation of methyl red dye by a novel actinobacterium *Zhihengliuella* sp. ISTPL4: kinetic studies, isotherm and biodegradation pathway. Environ. Technol. Innov. 26, 102348. https://doi.org/10.1016/j.eti.2022.102348.

Tamura, K., Nei, M., Kumar, S., 2004. Prospects for inferring very large phylogenies by using the neighbor-joining method. Proc. Natl. Acad. Sci. 101, 11030–11035. https://doi.org/10.1073/pnas.0404206101.

Tejashwini, P., Baker, S., Parashiva, J., Satish, S., 2026. Biodegradation potential of chlorpyrifos from soil microbiont *trichoderma asperellum* S8 and its biocontrol efficacy. Microbe 10, 100681. https://doi.org/10.1016/j.microb.2026.100681.

Tian, W., Chen, C., Lei, X., Zhao, J., Liang, J., 2018. CASTp 3.0: computed atlas of surface topography of proteins. Nucleic Acids Res. 46, W363–W367. https://doi.org/10.1093/nar/gky473.

Trott, O., Olson, A.J., 2010. AutoDock Vina: improving the speed and accuracy of docking with a new scoring function, efficient optimization, and multithreading. J. Comput. Chem. 31, 455–461. https://doi.org/10.1002/jcc.21334.

Vanommeslaeghe, K., Hatcher, E., Acharya, C., Kundu, S., Zhong, S., Shim, J., MacKerell Jr, A.D., 2010. CHARMM general force field: a force field for drug-like molecules compatible with the CHARMM all-atom additive biological force fields. J. Comput. Chem. 31, 671–690. https://doi.org/10.1002/jcc.21367.

Vanommeslaeghe, K., Raman, E.P., MacKerell Jr, A.D., 2012. Automation of the CHARMM General Force Field (CGenFF) I: bond perception and atom typing. J. Chem. Inf. Model. 52, 3144–3154. https://doi.org/10.1021/ci300363c.

Veerakumar, P., Sangili, A., Saranya, K., Pandikumar, A., Lin, K.C., 2021. Palladium and silver nanoparticles embedded on zinc oxide nanostars for photocatalytic degradation of pesticides and herbicides. Chem. Eng. J. 410, 128434. https://doi.org/10.1016/j.cej.2021.128434.

Verma, S., Singh, D., Chatterjee, S., 2020. Biodegradation of organophosphorus pesticide chlorpyrifos by *Sphingobacterium* sp. C1B, a psychrotolerant bacterium isolated from apple orchard in Himachal Pradesh of India. Extremophiles 24 (6), 897–908. https://doi.org/10.1007/s00792-020-01203-y.

Wang, B., Wu, S., Chang, X., Chen, J., Ma, J., Wang, P., Zhu, G., 2020. Characterization of a novel hyper-thermostable and chlorpyrifos-hydrolyzing carboxylesterase EstC: a representative of the new esterase family XIX. Pestic. biochem. physiol. 170, 104704.

Wang, C., Greene, D., Xiao, L., Qi, R., Luo, R., 2018. Recent developments and applications of the MMPBSA method. Front. Mol. Biosci. 4, 87. https://doi.org/10.3389/fmolb.2017.00087.

Wang, P., Rashid, M., Liu, J., Hu, M., Zhong, G., 2016. Identification of multi-insecticide residues using GC-NPD and the degradation kinetics of chlorpyrifos in sweet corn and soils. Food chem. 212, 420–426. https://doi.org/10.1016/j.foodchem.2016.05.008.

Wołejko, E., Łozowicka, B., Jabłońska-Trypuć, A., Pietruszyńska, M., Wydro, U., 2022. Chlorpyrifos occurrence and toxicological risk assessment: a review. Int. J. Environ. Res. Public Health N Hav. 19, 12209. https://doi.org/10.3390/ijerph191912209.

World Health Organization, 2020. Chemical safety: pesticides. https://www.who.int/news-room/questions-and-answers/item/chemical-safety-pesticides.

Wulandari, M., Zharfa, A.Z., Zuliandanu, D., Syukri, A., Nofrizal, N., Raja, P.B., 2025. The chloride mask in chemical oxygen demand determination of seawater and its validation. SJST 47.

Xu, L., Chen, S., Fu, W., Lin, X., Zhang, F., Qin, G., Yuan, Z., Huang, B., 2025. Environmental toxicant 2,3,7,8-tetrachlorodibenzo-p-dioxin induces non-obstructive azoospermia: new insights from network toxicology, integrated machine learning, and biomolecular modeling. Ecotoxicol. Environ. Saf. 295, 118173. https://doi.org/10.1016/j.ecoenv.2025.118173.

Yadav, I.C., Devi, N.L., Syed, J.H., Cheng, Z., Li, J., Zhang, G., Jones, K.C., 2015. Current status of persistent organic pesticides residues in air, water, and soil, and their possible effect on neighboring countries: a comprehensive review of India. Sci. Total Environ. 511, 123–137. https://doi.org/10.1016/j.scitotenv.2014.12.041.

Yadav, R., Pandey, V., Yadav, S.K., Khare, P., 2024. Comparative evaluation of biodegradation of chlorpyrifos by various bacterial strains: kinetics and pathway elucidation. Pestic. Biochem. Physiol. 203, 105989. https://doi.org/10.1016/j.pestbp.2024.105989.

Yue, C., Jia, N., Lv, X., Wang, S., 2023. Identification of two possible metabolic pathways responsible for the biodegradation of 3, 5, 6-trichloro-2-pyridinol in Micrococcus luteus ML. Biodegradation 34, 371–381. https://doi.org/10.1007/s10532-023-10023-8.

Zhang, Q., Li, S., Ma, C., Wu, N., Li, C., Yang, X., 2018. Simultaneous biodegradation of bifenthrin and chlorpyrifos by *Pseudomonas* sp. CB2. J. Environ. Sci. Health N Hav. B 53, 304–312. https://doi.org/10.1080/03601234.2018.1431458.

Zwietering, M.H., Jongenburger, I., Rombouts, F.M., Van't Riet, K J A E M, 1990. Modeling of the bacterial growth curve. Appl. Environ. Microbiol. 56, 1875–1881. https://doi.org/10.1128/aem.56.6.1875-1881.1990.